CHAPTER TWENTY-ONE

Nanopore Force Spectroscopy Tools for Analyzing Single Biomolecular Complexes

Olga K. Dudko,* Jérôme Mathé,† *and* Amit Meller‡

Contents

Abstract

The time-dependent response of individual biomolecular complexes to an applied force can reveal their mechanical properties, interactions with other biomolecules, and self-interactions. In the past decade, a number of single-molecule methods have been developed and applied to a broad range of biological systems, such as nucleic acid complexes, enzymes and proteins in the skeletal and cardiac muscle sarcomere. Nanopore force spectroscopy (NFS) is an emerging single-molecule method, which takes advantage of the native electrical charge of biomolecule to exert a localized bond-rupture force and measure the biomolecule response. Here, we review the basic principles of the method and discuss two bond breakage modes utilizing either a fixed voltage or a steady voltage ramp. We describe a unified theoretical formalism to extract

* Department of Physics and Center for Theoretical Biological Physics, University of California, San Diego, La Jolla, California, USA
† Laboratoire LAMBE (UMR 8587 —CNRS-CEA-UEVE), Université d'Evry-val d'Essonne, Evry, France
‡ Department of Biomedical Engineering and Department of Physics, Boston University, Boston, Massachusetts, USA

Methods in Enzymology, Volume 475
ISSN 0076-6879, DOI: 10.1016/S0076-6879(10)75021-7

kinetic information from the NFS data, and illustrate the utility of this formalism by analyzing data from nanopore unzipping of individual DNA hairpin molecules, where the two bond breakage modes were applied.

1. Introduction

The response of biomolecules to applied force can reveal their most fundamental mechanical properties, their interactions with other biomolecules or self-interactions, and in some cases, their structure. Thus, the trajectory describing the reaction of biomolecules to an applied force contains a wealth of information relevant to their biological function. Advances in single-molecule manipulation have made it possible to measure the forces and strains that develop during these processes with spatial resolution approaching the atomic level (sub-nm), and force sensitivity at the level of thermal fluctuations ($pN \sim k_B T/\text{nm}$ where k_B is the Boltzmann constant that yields the room temperature energy when multiplied with the temperature T). Micromanipulation techniques such as the atomic force microscope (AFM) and optical or magnetic tweezers (described elsewhere in this volume) are the most direct methods of exerting and measuring forces on biomolecules, and thus have been applied to a broad variety of biological systems, ranging from nucleic acids to enzymes to motor proteins (Cecconi *et al.*, 2005; Florin *et al.*, 1994; Gautel *et al.*, 1997; Greenleaf *et al.*, 2008; Kellermayer *et al.*, 1997; Liphardt *et al.*, 2001; Marszalek *et al.*, 1999; Merkel *et al.*, 1999; Schlierf and Rief, 2006; Schlierf *et al.*, 2004).

Nanopores represent a fundamentally different approach for obtaining force spectroscopy data (Wanunu and Meller, 2008). This emerging single-molecule technique utilizes native molecular electric charge to exert force on virtually any biomolecule when it is threaded through a single nanoscale constriction (Akeson *et al.*, 1999; Kasianowicz *et al.*, 1996, 2002; Meller *et al.*, 2000, 2001). In contrast to tweezers and AFM techniques, where force is applied mechanically to one point on the biomolecule by conjugation to a bead or cantilever, the force exerted on biomolecules using nanopore methods is both local to the region inside the pore and applied according to the molecule's effective charge in that region (Q_{eff}). Thus, this force is directly proportional to the electrical voltage drop across the pore (ΔV), $F = (Q_{\text{eff}}/l)\Delta V$, where l is the pore length. To quantify this force, the system's effective charge per unit length ($q_{\text{eff}} = Q_{\text{eff}}/l$) must be determined under the conditions used in each specific experiment. The pore constriction itself then exerts a negative and equal force ($-q_{\text{eff}}\Delta V$) on the molecule. The mechanical force appears as a localized shear force that destabilizes any biomolecular bonds or structures that will not pass easily through the pore, and can lead to their subsequent rupture.

Nanopore force spectroscopy (NFS) takes advantage of our ability to modify the applied voltage (or force) on molecules residing in the pore, in real-time, based on measurements of the ion-current (Bates *et al.*, 2003). The controlled application of local forces on single molecules (or a single-molecular complex) residing in the pore is designed to destabilize and rupture intermolecular bonds, as the response of the molecules is measured. Here we describe two main approaches to force spectroscopy using nanopores, involving either the application of a fixed force level or the application of linearly increasing force, to create mechanical tension. The application of force culminates in a molecular transition (or a ''rupture'') that is clearly observed in the nanopore system. Some examples for molecular transitions that can be probed are ligand–receptor dissociation, unfolding of a protein, or unzipping of nucleic acids. When performed at constant force (a constant voltage), these experiments directly probe the voltage-dependent lifetime of the system, $\tau(V)$. In contrast, the distribution of rupture voltages, $p(V)$, measured in experiments at a constant voltage-ramp speed needs to be processed to provide information about $\tau(V)$. In this chapter, we discuss these two bond breakage modes in the context of nanopore experiments, and show that the experimental output of these two modes is related quantitatively in an essentially model-free way. We describe a unified theoretical formalism to extract kinetic information from NFS data, and illustrate the utility of this formalism by analyzing data from nanopore unzipping of individual DNA hairpin molecules.

2. The Nanopore Method

In a nanopore experiment, an electrical force is applied directly to a charged biopolymer threaded through a molecular-sized constriction (a few nanometers), made in an thin insulating membrane separating two reservoirs of buffered salt solution typically 0.2–1 M of monovalent salt (Wanunu and Meller, 2008), as shown schematically in Fig. 21.1. The electric field applied across two electrodes placed on either side of the membrane results in a steady ionic countercurrent of negative and positive ions through the pore. Because the resistivity of the pore is orders of magnitude larger than the resistivity of the bulk solution, the electric field is highly localized to the pore region. When charged biopolymers randomly approach the pore vicinity, they are attracted into the pore region by a residual component of the electrical field, acting to funnel the molecules from bulk into the pore (Wanunu *et al.*, 2010). Once an end of the biopolymer is threaded into the pore, a much stronger force (roughly equal to $F = q_{\text{eff}}\Delta V$) is applied on the biopolymer, causing it to slide from one side of the membrane to the other. This process is usually referred

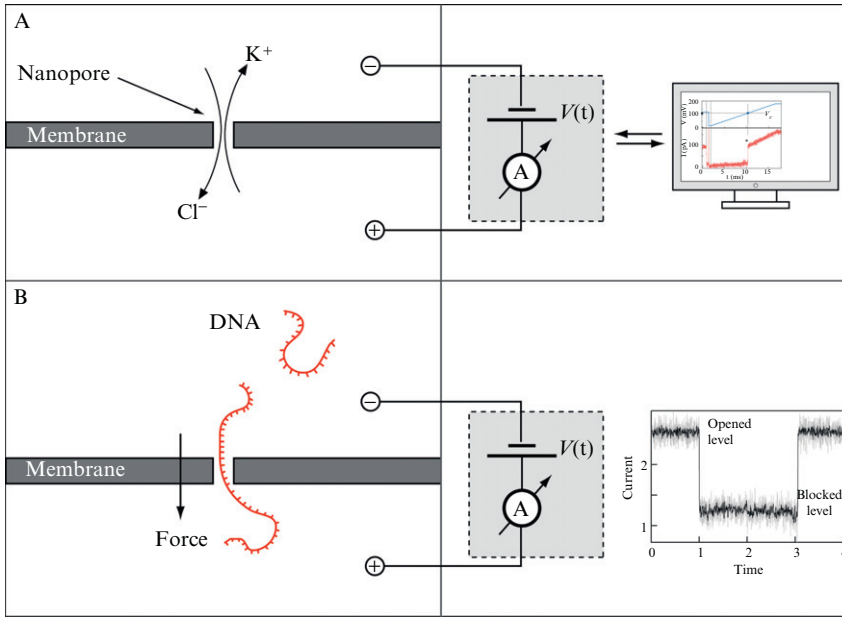

Figure 21.1 The nanopore method. (A) The ion-current flowing through a water-filled single nanoscale pore made in a thin membrane is measured using a pico-ampere electrometer. The voltage applied on the pore is dynamically controlled in real-time by a computer. (B) Insertion and threading of biopolymers cause abrupt blockades in the ion current, from the opened current state to the blocked current state, during the time in which the molecules remain in the pore. An electrical field applied across the membrane results in a strong force, driving the charged biopolymers from the negative to the positive chambers.

to as ''translocation'' (Meller, 2003). If the biopolymer's cross section is not uniform due to, for example, forming a hairpin or binding proteins, such that a local cross section is larger than the pore diameter, the translocation process will be interrupted until this ''obstacle'' is cleared. Formally, removal of these obstacles (i.e., unzipping of the hairpin, structures or stripping-off of bound proteins) is described by a crossing of a large energy barrier—much larger than that associated with moving an *unstructured* biopolymer through the pore. Since the waiting time associated with an energy barrier crossing increases exponentially with the barrier height, the characteristic translocation times of unstructured biopolymers (i.e., ssDNA, ssRNA, or polypeptides) are orders of magnitude smaller than the typical time required, for example, to unzip a hairpin of similar length.

In this chapter, we discuss two different kinds of bond-rupture measurements: pulling at a constant force, or with a linearly increasing force (i.e., with a constant force ramp). In nanopore experiments, these two types of

measurements can both be realized by dynamically modifying the voltage applied to the biomolecule, after it has been threaded to the pore, using a computerized system (Bates *et al.*, 2003). In the example shown in Fig. 21.2, the alpha-Hemolysin (α-HL) pore is utilized. The narrowest constriction of this protein channel ($\sim$1.4 nm) allows only single-stranded nucleic acids to be translocated, while double-stranded nucleic acids (i.e., hairpin structures) must be unzipped before translocation can proceed. In these experiments the current flowing through the pore is constantly measured, and the computerized data acquisition system is programmed to generate an output voltage signal triggered by an abrupt decrease in the pore current. Panel A depicts a typical unzipping event of a 10 base pair (bp) DNA hairpin where a step in the voltage is applied after molecular capture. The entry of the biomolecule into the pore creates an abrupt decrease in ion current, lowering it from the level of the opened pore to that of the blocked pore, which triggers the dynamic voltage control system. After a brief period of time (sufficient for threading the molecule up to the hairpin) the voltage is set to a constant level, V (90 mV in this case). Bond rupture (designated with an asterisk in Fig. 21.2) is signaled by a jump in the ion current at $t = t_U$. A histogram of hundreds of events collected in this manner is given, showing a peak at $\sim$1 ms and an exponentially decaying tail with a characteristic timescale of $\tau_U \sim 2.7$ ms.

In Panel B of Fig. 21.2, we display bond rupture using the *force-ramp* method. A linearly increasing voltage (''voltage ramp'') is applied after the initial threading of a single-stranded overhang into the nanopore. The pore current remains at the blocked level until the moment of rupture (designated with an asterisk), which is easily observed as an abrupt increase in ion current to the opened pore level. The voltage at which final rupture occurs is defined as V_U. Also displayed is a typical distribution of the rupture voltages for $\sim$1000 individual unzipping events similar to the one shown. In a typical experiment, distributions of unzipping events are collected for a wide range of different loading rates (ramp values).

To fully characterize bond-rupture kinetics, the measurements are performed over a broad range of force values (voltages) or force ramps (voltage ramps). The combined measurements represent the response force *spectrum* of the system. While, in principle, the fixed-force and the force-ramp methods formally report the same information on the system, there are practical differences between the two. For example, measuring bond breakage in the limit of small, constant forces could be extremely time-consuming and therefore often impractical. However, the same regime of bond rupture can be effectively ''scanned'' using the force-ramp method, saving much experimental time. Moreover, we show below that the force-ramp method effectively broadens the range of timescales accessible by the system. The unification of the two methods on a single ''master curve,'' discussed below, reinforces this point.

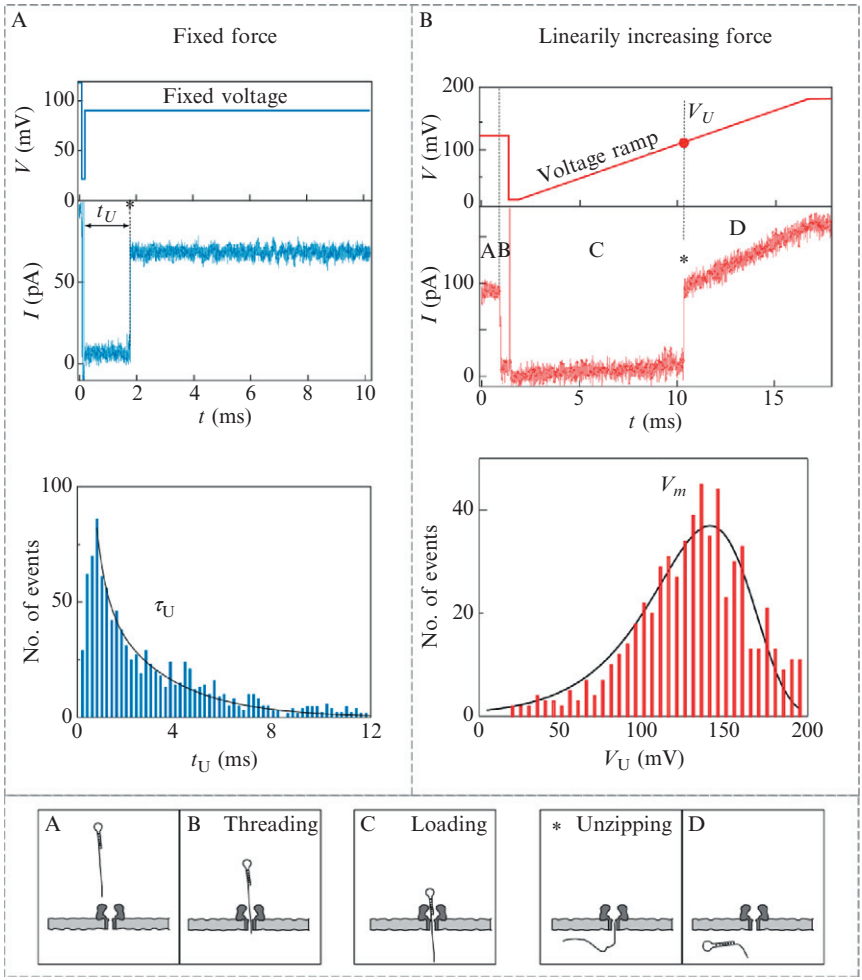

Figure 21.2 Implementation of force spectroscopy using nanopores. Two variants of the method are displayed: (A) Bond rupture using a step in the applied force (or voltage), where rupture is measured at a constant force, shown in blue. (B) Bond rupture under linearly increasing force (voltage ramp) shown in red. In both cases, a typical unzipping event (10 bp hairpin) is shown. Asterisks are used to denote the unzipping moment. In the fixed voltage case, the distribution of the unzipping time is measured for hundreds of events (see bottom histograms) yielding detailed characterization of the system response to force, through the timescale τ_U (fixed voltage) or the maximum voltage V_m (voltage ramp). Lower panel displays schematically the position of the hairpin with respect to the pore at each stage (A–D). Modified from Mathé *et al.* (2004) with permission.

2.1. Theory of force-driven molecular rupture

The wealth of high-resolution data collected in single-molecule force measurements has to be decoded in order to expose information about the mechanisms that drive biological processes. The interpretation of the experimental output in terms of underlying molecular interactions and structures often turns out to be a challenging task, because not only microscopic dimensions of these systems put the thermal fluctuations from the environment on an equal footing with the applied deterministic force, but also these experiments are often carried out under nonequilibrium conditions. Below we describe a recently introduced unified theoretical approach to analyzing data obtained in single-molecule force experiments.

Because thermal noise is an integral part of the molecular rupture process, biomolecular response to an applied force can only be described in probabilistic terms. Force-driven molecular rupture is viewed here as an irreversible molecular transition induced by a force F, during which the probability distribution of molecular configurations diffuses along the reaction coordinate x on a free-energy surface, $G(x) = G_0(x) - Fx$. The bare free-energy surface $G_0(x)$ is assumed to have a single well, a barrier at a distance $x^{\ddagger}$ from the well center, and an activation free energy, $\Delta G^{\ddagger}$. In the context of DNA unzipping in a nanopore (discussed later), the initial state, in the well of the free-energy surface, represents the single-stranded overhang of DNA threaded into the pore with the hairpin closed. Escape over the barrier involves unzipping of the double-stranded part of the DNA and the pore being cleared (Fig. 21.3A).

Even though this formalism assumes a single barrier and a single bound state, it can be applied to each individual transition in the case of multiple populated states, if the states can be resolved experimentally, for example, based on their molecular extensions along the reaction coordinate. The formalism is applicable to both the forward (e.g., unzipping or dissociation) and the backward (e.g., refolding or rebinding) transitions, as long as these transitions are quasi-irreversible.

We first consider the case of a constant force F accelerating the rate of molecular rupture. The theory (Dudko *et al.*, 2006) based on Kramers' picture of a diffusive barrier crossing (Kramers, 1940), predicts that for a sufficiently high barrier separating the unruptured state from the ruptured state, the lifetime (which is equal to the inverse escape rate $k(F)$) at a constant external force F is

$$\tau(F) = \tau_0 \left(1 - \frac{\nu F x^{\ddagger}}{\Delta G^{\ddagger}}\right)^{1-1/\nu} \exp\left\{-\beta \Delta G^{\ddagger}\left[1 - \left(1 - \frac{\nu F x^{\ddagger}}{\Delta G^{\ddagger}}\right)^{1/\nu}\right]\right\}. \quad (21.1)$$

Equation (21.1) expresses the force-dependent lifetime, which is the output of the constant-force experiment, in terms of three zero-force microscopic

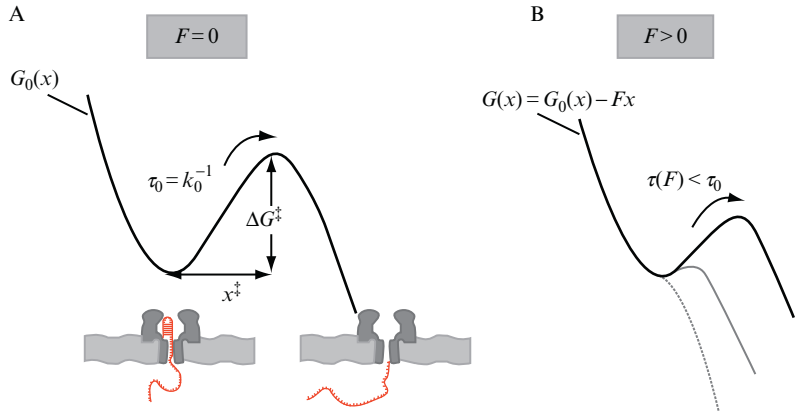

Figure 21.3 Conceptual picture of the molecular rupture under applied force viewed as a diffusive crossing of a barrier on a one-dimensional free-energy surface. (A) Intrinsic (i.e., zero-force) free-energy surface $G_0(x)$ with a well (bound state) and a barrier to quasi-irreversible rupture. In the context of the voltage-driven unzipping of individual DNA hairpin molecules in a nanopore, the well of the free-energy surface corresponds to the single-stranded DNA overhang threaded into the pore constriction with the folded hairpin trapped in the pore vestibule, while escape over the barrier involves the double-stranded part of the DNA being unzipped during its passage through the pore. (B) Free-energy surface $G(x)$ in the presence of an external force F. As the force increases, both the barrier height and the distance to the transition state decrease (gray line), and both eventually vanish (dotted line) when the well and the barrier merge at a critical force.

parameters: intrinsic lifetime τ_0, distance to the transition state $x^\ddagger$, and activation free-energy barrier $\Delta G^\ddagger$. Throughout this chapter, $\beta = (k_B T)^{-1}$ with k_B being the Boltzmann's constant and T the absolute temperature. Values $\nu = 2/3$ and $\nu = 1/2$ of the scaling parameter ν correspond to the linear-cubic surface $[G_0(x) = (3/2)\Delta G^\ddagger x/x^\ddagger - 2\Delta G^\ddagger (x/x^\ddagger)^3]$ and the harmonic-cusp surface $[G_0(x) = \Delta G^\ddagger (x/x^\ddagger)^2$ for $(x < x^\ddagger)$ and $-\infty$ for $x \geq x^\ddagger]$, respectively. For $\nu = 1$, or for $\Delta G^\ddagger \to \infty$ independent of ν, the phenomenological expression of Bell (1978) is recovered from Eq. (21.1).

Because Bell's formula, $\tau_{\text{Bell}}(F) = \tau_0 \exp(-\beta F x^\ddagger)$ (Eq. (21.1) with $\nu = 1$), predicts that the logarithm of the lifetime is a linear function of the applied force, any deviations from the linear dependence of $\ln \tau(F)$ on F have often been interpreted as a change in rupture mechanism (e.g., switching from one dominant barrier to another, or rebinding). However, Eq. (21.1) shows that simple microscopic models with a *single* barrier and a single bound state (like that depicted in Fig. 21.3) can explain nonlinearity in $\ln \tau$-versus-F plots without introducing additional assumptions of a change in mechanism. The reason for this limitation of the phenomenological Bell formula is the underlying assumption that the distance from the

well to the transition state, $x^{\ddagger}$, is independent of force. This assumption cannot be true for all forces: as can be readily seen by examining the behavior of any smooth one-dimensional potential (Fig. 21.3), the barrier and the well must move closer (solid gray line in Fig. 21.3B) as the force increases, because they eventually merge (dotted line in Fig. 21.3B) at a critical force when the barrier to rupture vanishes. As a result, $\ln \tau(F)$ must be a nonlinear function of F.

Equation (21.1) was derived for forces at which a significant barrier (several $k_{\mathrm{B}}T$) still exists, and this equation is thus valid only when the force is below a critical force at which the barrier vanishes, $F < \Delta G^{\ddagger}/\nu x^{\ddagger}$. To estimate the intrinsic (zero-force) parameters τ_0, $x^{\ddagger}$ and $\Delta G^{\ddagger}$, the logarithm of the lifetimes $\ln \tau(F)$ can be fitted using Eq. (21.1) with several trial values of ν. If the resulting estimates for the fitting parameters are relatively insensitive to ν over a range of ν values that all result in good fits, these estimates can be considered to be independent of the precise nature of the free-energy surface and thus meaningful.

When the force is ramped up linearly with time, such that the force loading rate $\dot{F} \equiv \mathrm{d}F/\mathrm{d}t = \text{const.}$ is constant, the distribution of forces at rupture is (Dudko *et al.*, 2006):

$$p(F|\dot{F}) = \frac{1}{\dot{F}\tau(F)} \exp\left(\frac{1}{\beta x^{\ddagger}\dot{F}\tau_0}\right) \exp\left[-\frac{1}{\beta x^{\ddagger}\dot{F}\tau(F)}\left(1-\frac{\nu F x^{\ddagger}}{\Delta G^{\ddagger}}\right)^{1-1/\nu}\right], \tag{21.2}$$

where $\tau(F)$ is the force-dependent lifetime of Eq. (21.1). For intermediate values of the force loading rate $\dot{F}$, the approximate analytical expressions for the mean rupture force $\langle F\rangle = \int F p(F|\dot{F})\,\mathrm{d}F$ and the variance $\sigma_{\mathrm{F}}^2 = \langle F^2\rangle - \langle F\rangle^2$ are (Dudko *et al.*, 2006):

$$\langle F\rangle \cong \frac{\Delta G^{\ddagger}}{\nu x^{\ddagger}}\left\{1-\left[\frac{1}{\beta\Delta G^{\ddagger}}\ln\frac{\mathrm{e}^{\beta\Delta G^{\ddagger}+\gamma}}{\beta x^{\ddagger}\dot{F}\tau_0}\right]^{\nu}\right\}, \tag{21.3}$$

$$\sigma_{\mathrm{F}}^2 \cong \frac{\pi^2}{6\beta^2 x^{\ddagger 2}}\left[\frac{1}{\beta\Delta G^{\ddagger}}\ln\frac{\mathrm{e}^{\beta\Delta G^{\ddagger}+\widetilde{\gamma}}}{\beta x^{\ddagger}\dot{F}\tau_0}\right]^{2\nu-2}. \tag{21.4}$$

Here $\widetilde{\gamma} = \gamma^2 - 3/\pi^2\psi''(1) \approx 1.064$, $\gamma \approx 0.577$, and $\psi''(1) \approx -2.404$ (Abramowitz and Stegun, 1972). When γ is formally set to zero, Eq. (21.3) is a good approximation for the maximum (mode) of the rupture force distribution.

The microscopic theory based on Kramers' picture of diffusive crossing of a barrier on a class of model potentials ($\nu = 1/2$ or $\nu = 2/3$ in Eqs. (21.3) and (21.4)) predicts that the mean rupture force (Eq. (21.3)) depends nonlinearly on the logarithm of the loading rate, $\dot{F}$, and the variance of the rupture force (Eq. (21.4)) is a function of the loading rate. In contrast, the phenomenological theory ($\nu = 1$ in (Eqs. (21.3) and (21.4)), based on Bell's postulate for the lifetimes, $\tau(F) = \tau_{\mathrm{Bell}}(F)$, leads to a linear dependence of the mean rupture force on the log-loading rate, and to the variance being independent of the loading rate. The predictions of the two approaches are tested against experimental data (Fig. 21.7) below.

Implicit in the derivation of Eqs. (21.2)–(21.4) is the quasi-adiabatic assumption that the force loading rate $\dot{F}$ is not too high so that by the time the barrier is so low that Kramers' theory is invalid, the survival probability (i.e., the probability to find the system unruptured) is effectively zero. If this quasi-adiabatic approximation is indeed valid, the following relation between the constant-force experiments (measuring $\tau(F)$) and constant-speed experiments (measuring $p(F|\dot{F})$) has been established (Dudko *et al.*, 2006, 2008):

$$\tau(F) = \frac{\int_F^\infty p(F')\,\mathrm{d}F'}{\dot{F}(F)p(F)}. \tag{21.5}$$

This equation predicts that the rupture force distributions $p(F|\dot{F})$ obtained at different values of the force-ramp speed $\dot{F}$ (right-hand side of Eq. (21.5)) can be directly transformed into the force dependence of the lifetime $\tau(F)$ (left-hand side of Eq. (21.5)) measurable in constant-force experiments. This mapping is independent of the nature of the underlying free-energy surface, and thus it relates the two types of experiments in a model-free way. Equation (21.5) predicts that data obtained at different loading rates must collapse onto a single master curve that yields the force dependence of $\tau(F)$ over a range of forces that may be wider than the range accessible in constant-force measurements. While the analytical solutions in Eqs. (21.2)–(21.4) were derived assuming a constant force loading rate, Eq. (21.5) holds also when the force loading rate, $\dot{F}$, is itself a function of force.

From Eq. (21.5) one can obtain an approximate but quite general relationship between the lifetime at a force equal to the mean rupture force and the variance of the rupture-force distribution (Dudko *et al.*, 2008):

$$\tau(\langle F\rangle) \approx \frac{1}{\dot{F}(F)}\left[\frac{\pi}{2}\left(\left\langle F^2\right\rangle - \langle F\rangle^2\right)\right]^{1/2}. \tag{21.6}$$

Whereas Eq. (21.6) gives an estimate for the $\tau(F)$ over a narrower range of F than does Eq. (21.5), the former should prove useful if the data permit estimates of only the mean and variance.

Force-dependent lifetimes $\tau(F)$ can be used to extract microscopic information *independent* of a particular model of the free-energy profile.

The following expression for the force-dependent lifetimes has been derived from Kramers high-barrier theory (Dudko *et al.*, 2008):

$$\tau(F) = \tau_0 \exp\left(-\beta \int_0^F \left\langle x^{\ddagger}(F')\right\rangle \mathrm{d}F'\right), \tag{21.7}$$

where $\left\langle x^{\ddagger}(F)\right\rangle$ denotes the difference in the average positions of the transition state and the bound state along the pulling coordinate as a function of force. A corollary of Eq. (21.7) is that the slope of $\ln \tau(F)$ versus F is a direct measure of how the distance between bound state and transition state changes with the force. Equation (21.7) can be viewed as the generalization of Bell's formula, $\tau_{\mathrm{Bell}}(F) = \tau_0 \exp(-\beta F x^{\ddagger})$, in the framework of Kramers theory. Equation (21.7) shows that Bell's formula is accurate only in the limited range of low forces when the distance from the well to the transition state can be considered to be independent of force (see Fig. 21.3B). Consequently, an uncritical use of the Bell's formula beyond a narrow range of low forces can lead to significant errors in the estimated intrinsic lifetime τ_0 and the distance to the transition state $x^{\ddagger}$.

In nanopore unzipping experiments, the applied voltage V is analogous to the applied mechanical force F in pulling experiments (e.g., those using AFMs or optical tweezers). The voltage drop across the membrane-spanning nanopore results in an electric field that generates a mechanical force on the charged DNA strand threaded into the nanopore (Fig. 21.3A). To adapt the above formalism to nanopore-unzipping experiments, the voltage $V^{\ddagger} = k_{\mathrm{B}}T/Q_{\mathrm{eff}}$ can be defined as the characteristic of the transition state, where Q_{eff} is the effective charge of the DNA inside the pore (Mathé *et al.*, 2004). Equations (21.1)–(21.7) can then be used by making the following change of variables:

$$\beta F x^{\ddagger} \rightarrow V/V^{\ddagger}, \tag{21.8}$$

and with $\dot{F} = \mathrm{d}V/\mathrm{d}t$ being the voltage-ramp speed.

2.2. Analysis of NFS experiments

2.2.1. Analysis of constant-force experiments

Voltage dependence of the lifetime obtained in constant-voltage measurements can be interpreted in microscopic terms simply by least-squares fitting the data with Eq. (21.1) at several fixed values of v. If the resulting parameters τ_0, $x^{\ddagger}$, and $\Delta G^{\ddagger}$ are relatively insensitive to v in the range of $1/2 \leq v \leq 2/3$, and thus to the precise shape of the underlying free-energy surface, these parameters may be considered meaningful. Alternatively, Eq. (21.7) that is formally exact within the framework of Kramers' theory

can be used to extract information about the transition state as a function of force from the lifetimes, *independent* of the shape of the free-energy surface.

2.2.2. Analysis of force-ramp experiments

Two complementary approaches can be used to extract microscopic information from rupture-voltage distributions obtained in a constant-force-ramp experiment. In the first approach, a maximum-likelihood (ML) formalism is used to fit with Eq. (21.2) all rupture-voltage histograms collected at one or (preferably) several ramp speeds $\dot{F}$ (Dudko *et al.*, 2007). In the second approach, rupture-voltage histograms are transformed according to Eq. (21.5) into the voltage dependence of the lifetime, and the resulting lifetimes can be analyzed as described above in section 2.2.1 (Dudko *et al.*, 2008). Implementation of these two approaches is discussed below.

2.2.2.1. Maximum-likelihood analysis of force-ramp experiments Consider a series of constant force-ramp speed experiments at several ramp speeds $\dot{F}_j$ ($j = 1, \ldots, N$). Molecular rupture will be observed at different forces F_{ij} ($i = 1, \ldots, M_j$). The likelihood function L needs to be maximized with respect to a set of model parameters, $\{\alpha\}$. L can be expressed in terms of the rupture force distribution $p(F|\dot{F})$ at ramp speed $\dot{F}$ as

$$L = \prod_{j=1}^{N} \prod_{i=1}^{M_j} p(F_{ij}|\{\alpha\}; \dot{F}_j). \tag{21.9}$$

To implement this approach, it is convenient to have an analytical expression for $p(F|\dot{F})$. The unified formalism described above provides such an expression in Eq. (21.2) in terms of the model parameters, namely the intrinsic lifetime τ_0, the location of the transition state $x^{\ddagger}$, and the activation free energy $\Delta G^{\ddagger}$. Given experimental measurements, optimal values of τ_0, $x^{\ddagger}$, and $\Delta G^{\ddagger}$ can be found by maximizing L or, equivalently, $\ln[L]$ for different fixed values of ν. As in the case of the constant-voltage data analysis, if the resulting parameters $\{\tau_0, V^{\ddagger}, \Delta G^{\ddagger}\}$ are relatively insensitive to the value of ν in the range $1/2 \leq \nu \leq 2/3$, then they can be considered meaningful.

2.2.2.2. Transformation of rupture-voltage histograms into voltage dependence of lifetime The histogram transformation approach is based on the mapping equation, Eq. (21.5), which transforms rupture-voltage histograms measured at different voltage-ramp speeds directly into voltage dependence of the rupture lifetime. The transformation of histograms using Eq. (21.5) is implemented as follows. Consider a rupture force histogram at

the force-ramp speed, $\dot{F}$. The histogram contains N bins of width ΔF, starts at F_0 and ends at $F_N = F_0 + N\Delta F$, and has N_{tot} total number of counts. Let the number of counts in the ith bin be C_i, resulting in a height $p_i = C_i/(N_{tot}\Delta F)$ in the normalized force distribution. Then the lifetime at the force $F_0 + (k - 1/2)\Delta F$ is

$$\tau[F_0 + (k-1/2)\Delta F] = \frac{\left(p_k/2 + \sum_{i=k+1}^{N} p_i\right)\Delta F}{\dot{F}(F_0 + (k-1/2)\Delta F)p_k}, \tag{21.10}$$

where $k = 1, 2, \ldots$ Eq. (21.10) is simply a discrete version of Eq. (21.5).

If the histograms do collapse onto a single master curve, one immediately obtains the force (voltage) dependence of the molecular bond lifetime, $\tau(F)$, or equivalently the rate of rupture, $k(F) = 1/\tau(F)$. The force dependence of the lifetime can now be interpreted in microscopic terms in exactly the same way as the lifetimes that were measured directly in constant-voltage experiments, namely by performing a least-squares fit with Eq. (21.1), or by using a model-independent approach in Eq. (21.7). If the histograms transformed by Eq. (21.5) do not collapse onto a single master curve, then the mechanism of rupture cannot be described as an irreversible, quasi-adiabatic escape over a single barrier. Such behavior may also be evident in non-exponential distributions of the lifetimes in constant-force experiments.

3. DNA Unzipping Kinetics Studied Using Nanopore Force Spectroscopy

The unzipping of double-stranded nucleic acids occurs in a large number of cellular processes, including DNA replication, RNA transcription, translation initiation, and RNA interference. The forces and timescales associated with the breakage of the bonds stabilizing the secondary and tertiary structures of nucleic acids can now be studied at the single-molecule level, revealing information masked heretofore by ensemble averaging, including short-lived intermediate states and multistep kinetic processes. Here we describe the use of nanopores to directly apply and measure unzipping forces on individual DNA and RNA molecules, eliminating the need for molecular linkers, for surface immobilization of the molecules, and for global application of force.

The protein pore α-HL is nearly ideal for nucleic acid unzipping studies. Its heptameric structure (Song *et al.*, 1996), composed of cap and stem portions, has been shown to be highly stable even under high temperatures, voltage gradients (Kang *et al.*, 2006), and a wide range of ionic strengths (i.e., 0.25–2 *M* KCl) (Jan Bonthuis *et al.*, 2006). The cap portion of α-HL, which is usually assembled on the "*cis*" side of the membrane, contains a

wide vestibule-like mouth, which can accommodate double-stranded nucleic acids. The stem portion, which spans the phospholipid membrane, is a nearly cylindrical water-filled channel with an inner diameter ranging from 1.4 to 2.2 nm (Song *et al.*, 1996). It therefore geometrically permits the passage of single-stranded DNA or RNA molecules, but blocks the translocation of double-stranded nucleic acids.

Sauer-Budge *et al.* (2003) have demonstrated that a DNA duplex molecule (composed of a 100-mer DNA oligonucleotide hybridized to a matching 50-mer oligonucleotide, such that a 50-mer 3′ single-stranded overhang is formed), must be unzipped when the 3′ overhang is threaded through the pore. A quantitative PCR analysis showed that while both the 50-mer and 100-mer oligonucleotides were present in the *cis* chamber, only the 100-mer oligonucleotide was found in the *trans* chamber, after the detection of hundreds of nanopore blockade events. This observation is explained if unzipping occurred at the pore, leaving all 50-mer oligonucleotides in the *cis* chamber while the 100-mer oligonucleotides passed through the pore to the *trans* side (Sauer-Budge *et al.*, 2003). Furthermore, the distribution of nanopore blockade durations (or dwell-times) displayed a characteristic mean time of $\sim$435 ms, orders of magnitude longer than the timescale associated with the translocation of single-stranded DNAs of comparable length. Introducing a 6-base mismatch in the duplex region of the hybridized sample resulted in a shortening of the characteristic timescale by more than a factor of two (Sauer-Budge *et al.*, 2003).

Mathé *et al.* (2004, 2006) employed NFS to study the properties of the unzipping kinetics of DNA hairpin molecules. They systematically probed the unzipping time probabilities of three DNA hairpin molecules composed of a duplex stem region (of 10 bp, 9 bp, which is a 10 bp plus a mismatch at the fifth base pair, or 7 bp, all with a capping 6-base loop) attached to a 3′ poly$(dA)_{50}$ overhang. The poly$(dA)_{50}$ tail is used to insert the molecules into the pore and thus apply the electric force primarily to the duplex region. The unzipping kinetics was probed over a wide range of voltage (30–150 mV) and at several temperatures (from 5 to 20 °C). The temperature dependence will be discussed later on. Figure 21.2 displays a typical unzipping event using this technique at a constant unzipping voltage, where the event's unzipping time is denoted t_U. To obtain the *characteristic* unzipping time (τ_U) approximately 1500 events were accumulated at each voltage leading to the unzipping time distribution. Figure 21.4 displays the time-cumulative distribution for the three hairpin molecules probed at a constant voltage of 120 mV and at 15 °C. These measurements revealed that a single base pair mismatch strongly shifts the unzipping timescale towards shorter times and can therefore be easily detected using unlabeled and unmodified DNA hairpin and DNA hybrids.

The cumulative unzipping time distributions were fitted well with mono-exponential functions (shown as dashed line in Fig. 21.4), indicating first-order

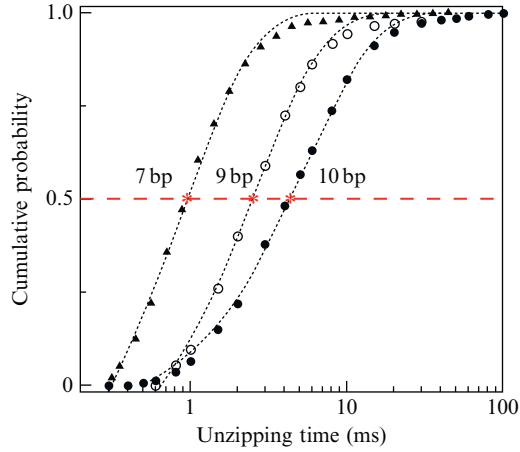

Figure 21.4 Detecting single base mismatches in unlabeled DNA hairpins. The normalized cumulative distributions of the unzipping time measured using DVC at 120 mV and 15 °C, for 10, 9 (10 bp with a mismatch), and 7 bp DNA hairpins (solid circles, empty circles, and triangles respectively). Mono-exponential probability distribution fits (dashed lines) yield characteristic unzipping timescales (~5, 3, and 1 ms for the 10, 9, and 7 bp hairpins, respectively) used to discriminate between the hairpins.

rate kinetics. The characteristic time of these exponential fits is the mean unzipping time τ_U and its dependence on voltage V is shown in Fig. 21.5 as a semilogarithmic plot. When this characteristic time versus voltage plot was fitted using the phenomenological Bell model, $\tau_U(V) = \tau_0 \exp(-V/V^{\ddagger})$, where $V^{\ddagger}$ contains the effective charge (as explained above) on which the electric force is applied and τ_0 contains the energy barrier height of the duplex region, it was found that $V^{\ddagger}$ does not depend on the duplex region (the slopes are the same) leading to $V^{\ddagger} = 22 \pm 2$ mV and thus an effective charge of $Q_{\text{eff}} = 1.13 \pm 0.1e$, in good agreement with initial experimental determinations by Sauer-Budge *et al.* (2003).

DNA hairpin unzipping measurements were also performed using voltage-ramp measurements, as explained in Fig. 21.2. Using ramp voltage has several practical advantages over constant-voltage measurement. Most importantly, constant-voltage experiments appear to be much more time consuming as compared to voltage-ramp experiment. This feature is a direct consequence of the roughly logarithmic dependence of V_m (proportional to time with linear ramp voltage) on the ramp as the unzipping timescale in a constant-voltage experiment depends roughly exponentially on the voltage applied. ML analysis and Eq. (21.2) can be used to fit NFS voltage ramp data. Below we also demonstrate how to convert, using Eq. (21.5), the voltage-ramp data directly into the voltage dependence of the unzipping times measured at constant voltage.

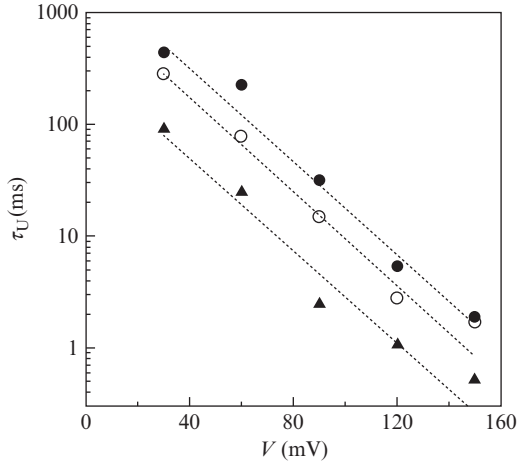

Figure 21.5 Dependence of the characteristic unzipping timescale on the voltage measured using dynamic voltage control, for 10, 9 (10 bp with a mismatch), and 7 bp DNA hairpins (solid circles, empty circles, and triangles respectively). As a first approximation, all molecules follow a mono-exponential dependence on V with the same slope. Reproduced with permission from Mathé *et al.* (2004).

3.1. Maximum-likelihood analysis of voltage-ramp data

Over 32 independent DNA hairpin unzipping data sets, obtained for different ramp values, were used to construct unzipping voltage histograms and were globally fit using Eq. (21.2) by maximizing the likelihood function, Eq. (21.9). Figure 21.6 presents the results of the fits using Eq. (21.2) with $\nu = 2/3$ (linear-cubic model) on all ramp speeds of 12 V/s or less. Ramp speeds above 12 V/s were used for further validation of the global fit. Histogram colors represent four voltage-ramp ranges (see caption). As summarized in Table 21.1, the two microscopic theories ($\nu = 2/3$ and $\nu = 1/2$ in Eq. (21.2)) produce consistent estimates for the model parameters. ML fitting parameters of the phenomenological theory ($\nu = 1$ in Eq. (21.2)) are also included for comparison.

Figure 21.7 shows the most probable unzipping voltage V_m as a function of the voltage-ramp speed. The markers represent the experimental data, and the solid line is the theoretical prediction using microscopic theory (Eq. (21.3) with γ set to 0 and $\nu = 2/3$) with ML parameters as in Table 21.1. The dashed line is a fit with the phenomenological model (Eq. (21.3) with $\nu = 1$), where V_m is logarithmically dependent on the voltage-ramp speed (when only intermediate and high-voltage ramps are used). In order to account for the observed curvature in the experimental data at low ramp speeds one needs to add to the phenomenological rate model additional molecular processes, such as hairpin-rezipping or switching between multiple states that cannot be

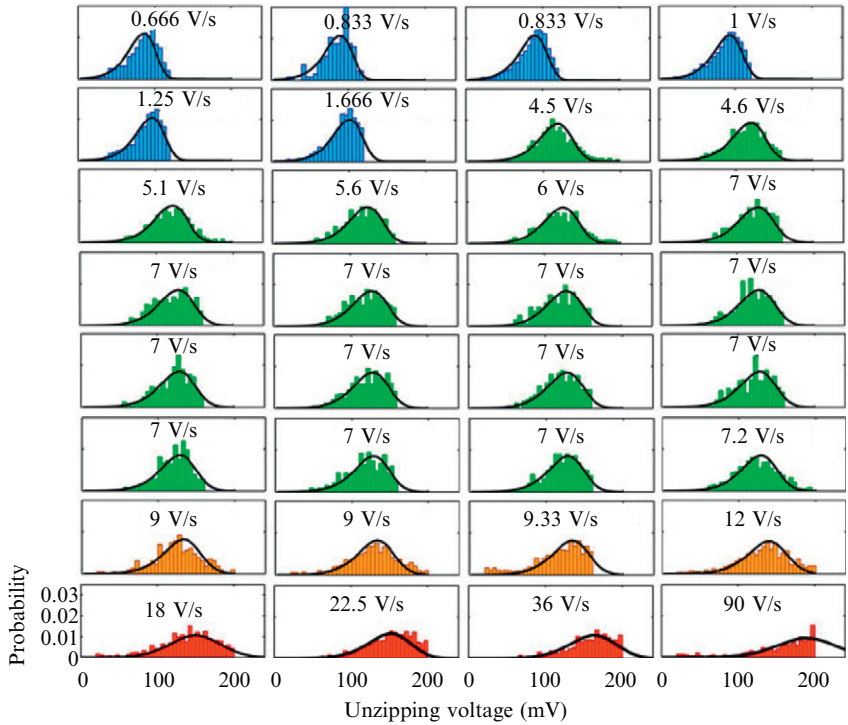

Figure 21.6 Distribution of the unzipping voltage from experiment (histograms) and theory (lines). Theoretical distributions were obtained by maximum-likelihood (ML) global fit of histograms at ramp speed of 12 V/s or less to Eq. (21.2) with $v = 2/3$ (linear-cubic model); the result for $v = 1/2$ (linear-cubic model, not shown) is very similar. The likelihood function, Eq. (21.9), was maximized numerically with respect to the model parameters. Experimental data collected at ramp speeds above 12 V/s (in this regime the DNA hairpin was still intact when the maximum voltage 0.2 V had been reached) were not used in the fit. The microscopic theories reproduce the measured distributions of unzipping voltages very well both in the regime used for the fit and outside that regime. The phenomenological model (fit not shown) with the estimates obtained from the global ML fit was found to be accurate at low ramp speeds, whereas at higher speeds the deviations were substantial. Colors reflect different ranges of the ramp speed and correspond to those in Figs. 21.7 and 21.8. Data reproduced from Dudko *et al.* (2007) with permission.

represented by a single energy well model (e.g., Fig. 21.3). In contrast, the microscopic models (Eq. (21.3) with $v = 2/3$ and $v = 1/2$) captures the nonlinearity in V_m as a function of $\log \dot{V}$, without the need to make any assumptions beyond a single-well energy landscape. Additionally, it can be verified (Dudko *et al.*, 2007) that the variance, σ_V^2, of the unzipping voltage distributions exhibits a noticeable increase with the ramp speed, in agreement with the microscopic theories [Eq. (21.4) with $v = 1/2$ and $v = 2/3$].

Table 21.1 Maximum-likelihood estimates for the kinetic parameters for nanopore unzipping of DNA

ν	$V^{\ddagger}$ (mV)	$\Delta G^{\ddagger}$ ($k_B T$)	τ_0 (s)
1	21.7	–	1.6
2/3	12.7	10.5	8.3
1/2	9.9	11.9	20

Estimates were obtained from data in Fig. 21.6 at ramp speeds 12 V/s or less by maximizing the likelihood function in Eq. (21.9) with the expression in Eq. (21.2) for the unzipping voltage distributions.

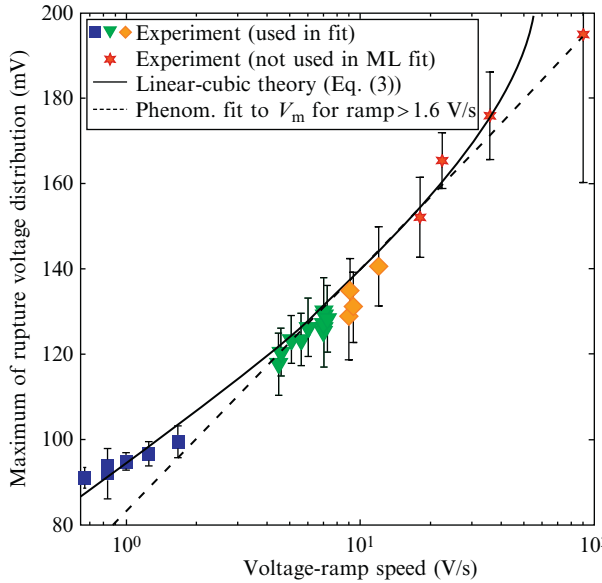

Figure 21.7 Dependence of the maximum V_m of the unzipping voltage distribution on the voltage-ramp speed from experiment (markers) and theory (lines, Eq. (21.3) with γ set to 0). Model parameters for the linear-cubic theory (solid line, Eq. (21.3) with $\nu = 2/3$) were obtained from global ML fit, see Fig. 21.6 and Table 21.1; result for the harmonic-cusp theory (Eq. (21.3) with $\nu = 1/2$, not shown) is very similar. Dashed line is the least-squares fit of the maxima of unzipping voltage distributions to the phenomenological model (Eq. (21.3) with $\nu = 1$) for ramp speeds >1.6 V/s. Color coding as in Fig. 21.6. Data reproduced from Dudko *et al.* (2007) with permission.

3.2. Histogram transformation method

Quantitatively relating the constant-voltage data to the voltage-ramp data using Eq. (21.5) and its discrete analog, Eq. (21.10) provides a simple way to obtain the voltage-dependent lifetime $\tau(F)$ directly from the voltage-ramp

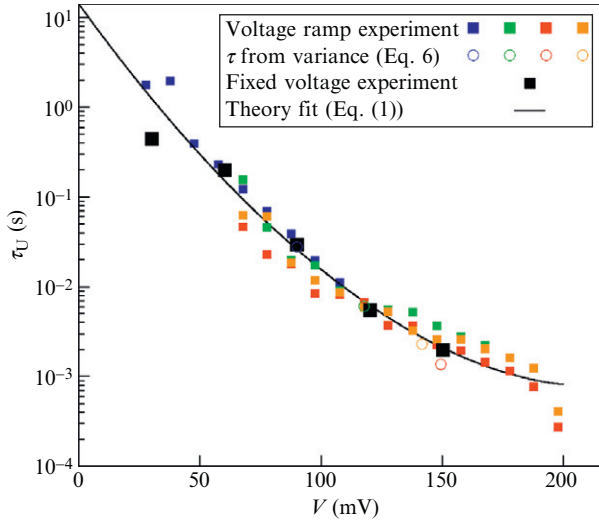

Figure 21.8 Comparison of DNA hairpin unzipping lifetimes τ_U obtained from transformation of the voltage-ramp experiments according to Eq. (21.5) (solid squares) for ramp speeds from 0.83 to 18 V/s, or from the distributions' variance analysis (Eqs. (21.6) and (21.7)). Colors indicate the range of ramp speeds as in Fig. 21.6. Constant voltage measurements of the unzipping lifetime are shown in black. Least-squares fit of the collapsed histograms to Eq. (21.1) with $\nu = 1/2$ displays remarkable agreement with data over a broad timescale range (black line). The fit with $\nu = 2/3$ (not shown) is comparable. Modified from Dudko *et al.* (2008) with permission.

data. Figure 21.8 is an illustration of the utility of Eq. (21.5) for this purpose. Not only do the lifetimes $\tau(F)$ obtained from histograms at different ramp speeds collapse onto the same curve (colored symbols), but there is also excellent agreement with DNA unzipping lifetimes obtained by an *independent set of measurements* of $\tau(F)$ using constant voltages (open circles). The lifetime obtained from the mean and variance using Eq. (21.6) (filled circles) is also found to agree with the constant-voltage experiments.

Now that the voltage dependence of the lifetime has been obtained from rupture-voltage histograms, the procedure of interpreting this dependence in microscopic terms can be implemented. It is clear from Fig. 21.8 that deviations from the mono-exponential dependence of the lifetime on the voltage are present when the voltage exceeds ~125 mV. The microscopic models ($\nu = 1/2$ and $\nu = 2/3$) allow us to perform a least-squares fit of the data with Eq. (21.1) over the entire range of accessible voltage, producing the following kinetic parameters: $\tau_0 = 14.3$ s, $V^\ddagger = 11.1$ mV, and $\Delta G^\ddagger = 11.9 k_B T$ for $\nu = 1/2$, and $\tau_0 = 9.6$ s, $V^\ddagger = 12.8$ mV, and $\Delta G^\ddagger = 10.4 k_B T$ for $\nu = 2/3$, in good agreement with the values of the ML global analysis in Table 21.1. Collapsed data collected at different ramp

speeds probe different ranges of the DNA unzipping lifetime. Taken together, they span four orders of magnitude of the bond-rupture lifetime. Furthermore, Fig. 21.8 shows that, although constant-voltage data (open circles) were not used in the fit, the data are accurately predicted by Eq. (21.1).

It can be verified (Dudko *et al.*, 2008) that the microscopic theory in Eq. (21.1) is able to accurately *predict* the original rupture-voltage distributions when the parameters of the least-squares fit of the collapsed distributions with Eq. (21.1) are used. Thus in this case, the histogram transformation procedure gives essentially the same information as the more sophisticated ML method, but is simpler to implement.

3.3. Temperature rescaling of unzipping data

Another way to probe a broader range of unzipping lifetimes is to vary temperature. As shown in Fig. 21.9 (inset) for a constant voltage experiment, changing the temperature by 5 °C is sufficient to shift the characteristic unzipping time by a factor of 2–5. One can consider that changing temperature has a similar effect as changing voltage (both modify the effective energy

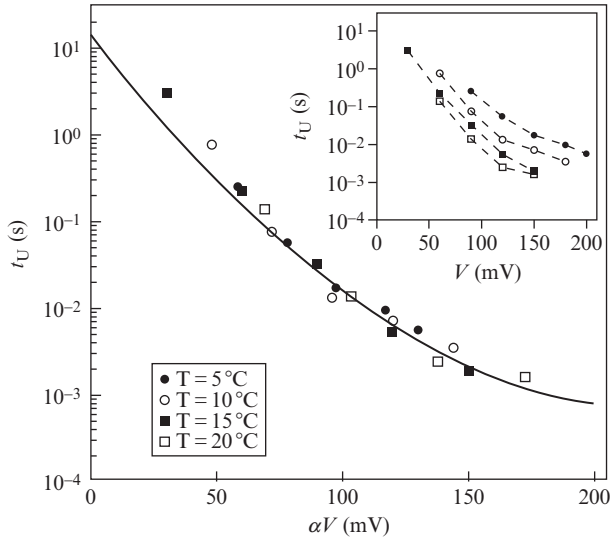

Figure 21.9 Rescaling of constant voltage unzipping time obtained at different temperatures. Lifetime $\tau(V)$ of the DNA hairpin as a function of the rescaled applied voltage V. The rescaling parameter was calculating in order to minimize the distance between points and then collapse all four temperature curves onto a single curve. The line represents Eq. (21.1) with the parameters obtained from Fig. 21.8 data points fit. *Inset*: Unzipping lifetime versus voltage at different temperatures (5, 10, 15, and 20 °C) without rescaling.

barrier), but they are not completely uncoupled since temperature can, in principle, alter the DNA effective charge. However, to first approximation, we can rescale the voltage by a proportionality parameter α as a function of temperature in order to collapse all four temperatures on a single curve while keeping the 15 °C data unchanged ($\alpha = 1$). Since the absolute temperature range is small, it is difficult to extract the dependence of this rescaling parameter on the temperature. We therefore choose to collapse the curves by minimization of the distance between each data point. Figure 21.9 presents the result of this collapse. In addition, we added to this graph the theoretical prediction from Eq. (21.1) using the parameters found previously and displayed in Fig. 21.8. One can see that the rescaled data match the theoretical prediction excepted at low voltages where the timescales are on the order of 1 s and thus large statistics are hard to attain. This consistency shows that the unzipping lifetime range can be broadened by changing temperature and, even better, by performing ramp experiments at various temperatures.

4. Conclusions and Summary

Direct probing of molecular bond strengths reveals biologically relevant information on a molecule's structure and function, and thus has been the objective of multiple single-molecule techniques. NFS utilizes the native electric charge of biomolecules to directly exert forces when a biomolecule is threaded through a nanoscale constriction. Because the method does not involve the formation of a physical attachment between the biomolecule and the pore, biomolecules do not require any modifications, such as attachment of long molecular handles. This highly simplifies experimental procedures and their analysis. In the nanopore method, the pore itself exerts a shear force on those parts of the biomolecular complex that do not fit inside the pore. NFS utilizes these advantages to locally rupture bonds and directly measure $\tau(V)$ and $p(V)$, two important indicators of bond stability.

The process of bond rupture is often described by diffusive crossing of an activation free-energy barrier, where the bound state refers to the unperturbed system, and the unbound state describes the ruptured bond. In many cases, the bound and unbound states are separated by a large energy barrier (many $k_B T$) and the system remains stable over long periods of time. The energy barrier height and thus bond stability are reduced by an external application of force, effectively catalyzing the molecular transition. Force spectroscopy probes a system's response over a broad spectrum of forces by measuring either the distribution of bond times-to-rupture at each given force, or the rupture-force distribution at a given force-ramp speed. Either measurement allows mapping of the system's energy landscape, and extrapolation of the nonequilibrium transition rate to the equilibrium transition rate.

To interpret the experimental output in terms of the underlying molecular properties, we have described here a unified theory for a class of single-barrier free-energy landscape models. While this theory describes a simple case of a single, high energy barrier, it yields closed-form analytical solutions for the experimental observables. The resulting theoretical predictions can be readily used to fit the voltage-dependent bond lifetimes measured for constant force (using Eq. (21.1)), and to employ the powerful ML analysis of the rupture-voltage distributions measured for a constant force ramp (using Eq. (21.2)). The result of these analyses is a set of intrinsic physical parameters characterizing the system, namely the activation free-energy barrier height, its position with respect to the bound state, and the characteristic lifetime (or, equivalently, the inverse intrinsic rate) of the system. It has also been shown that the rupture-voltage histograms obtained at different voltage-ramp speeds can be transformed to determine the voltage-dependence of the bond lifetimes measurable at constant voltage (Eq. (21.5)). This transformation is independent of the functional form of the free-energy landscape, and is valid if the rupture-voltage kinetics at constant voltage is well represented by a single exponential. Although this formalism was developed to describe irreversible rupture, it is applicable to both forward and reverse transitions as long as they can be resolved experimentally.

In this chapter we have illustrated the principles of NFS by focusing on DNA hairpin unzipping kinetics. We show that constant voltage and steady voltage-ramp experiments can be mapped onto the same rupture-time versus voltage curve (Fig. 21.8), which can then be interpreted in microscopic terms using a unified theory (Eq. (21.1)), providing insight into the system's underlying energy landscape and rates. As explained, the single well model applies only to short hairpins for which the unzipping process can be considered to occur in a single prominent step. This should also apply to simple DNA–protein complexes. The unzipping of longer hairpins or duplex regions involves a more complex process, which may entail energy landscapes with several consecutive energy wells. A similar consideration may apply to sequences containing, for example, several GC rich regions. Recently Monte-Carlo simulations of long sequences have been performed (Bockelmann and Viasnoff, 2008) showing that NFS is able to detect the position of a large barrier in a DNA-unzipping free-energy landscape.

The NFS method is quite general and already has been applied to other biomolecular systems. For example, Hornblower *et al.* (2007) have recently used NFS to study the interactions of Exonuclease I with single-stranded DNA molecules. NFS data can be extrapolated to zero voltage (or zero-force) and be used to measure the dissociation and association constants of the system. While most of the work presented here utilized the membrane channel α-HL, the fragility of the bilayer membrane has limited these measurements to relatively small forces (up to a few tens of pN). A wider range of biomolecular complexes, such as long DNA/RNA molecules or

proteins can be studied using NFS if this limitation is removed. The recent progress in fabrication and characterization of synthetic nanopores, specifically nanopores made in thin inorganic membranes (Kim *et al.*, 2006; Li *et al.*, 2001; Storm *et al.*, 2003), has generated vast possibilities for NFS. Solid-state nanopores offer superior mechanical, electrical, and chemical robustness over lipid bilayers used with biological pores. Thus, larger force ranges and a variety of chemical conditions, including extreme pH or denaturants can be used (Wanunu and Meller, 2008). Additionally, a solid-state nanopore can now be tailored to any desired dimension, down to $\sim$1 nm diameter (Kim *et al.*, 2006). Thus a much broader range of bimolecular complexes can be studied, under broader experimental conditions. Specifically, double-stranded DNA (Gershow and Golovchenko, 2007; Heng *et al.*, 2004; Storm *et al.*, 2005; Wanunu *et al.*, 2008), single-stranded nucleic acids and unzipping of duplex regions (Fologea *et al.*, 2005; McNally *et al.*, 2008), DNA–protein interactions as well as DNA–drug interactions can be studied in great detail (Smeets *et al.*, 2009; Wanunu *et al.*, 2009). These developments will undoubtedly be employed for high-throughput NFS analyses of a broad range of biological systems.

ACKNOWLEDGMENTS

A. M. acknowledges fruitful collaboration and discussions with Daniel Branton, Yitzhak Rabin, Mark Akeson, Breton Hornblower, and Anatoly Kolomeisky. O. K. D. is grateful to Attila Szabo and Gerhard Hummer for an exciting collaboration on the theory of single-molecule force spectroscopy. We thank Meni Wanunu for constructive and insightful comments on this manuscript. O. K. D. is supported by the National Science Foundation CAREER Award (MCB-0845099), a Hellman Faculty Fellows Award and the National Science Foundation Grant to the Center for Theoretical Biological Physics (PHY-0822283). J. M. acknowledges financial support from ANR PNANO grant ANR-06-NANO-015-02. A. M. acknowledges grant support from the National Science Foundation (PHY-0646637), the National Institute of Health (HG-004128 and GM-075893), and the Human Frontier Science Program (RGP0036).

REFERENCES

Abramowitz, M., and Stegun, I. A. (1972). Handbook of Mathematical Functions. Dover, New York.

Akeson, M., Branton, D., Kasianowicz, J., Brandin, E., and Deamer, D. (1999). Microsecond time-scale discrimination among polycytidylic acid, polyadenylic acid, and polyuridylic acid as homopolymers or as segments within single RNA molecules. *Biophys. J.* **77,** 3227–3233.

Bates, M., Burns, M., and Meller, A. (2003). Dynamics of single DNA molecules actively controlled inside a membrane channel. *Biophys. J.* **84,** 2366–2372.

Bell, G. I. (1978). Models of the specific adhesion of cells to cells. *Science* **200,** 618–627.

Bockelmann, U., and Viasnoff, V. (2008). Theoretical study of sequence-dependent nanopore unzipping of DNA. *Biophys. J.* **94,** 2716–2724.
Cecconi, C., Shank, E. A., Bustamante, C., and Marqusee, S. (2005). Direct observation of the three-state folding of a single protein molecule. *Science* **309,** 2057–2060.
Dudko, O. K., Hummer, G., and Szabo, A. (2006). Intrinsic rates and activation free energies from single-molecule pulling experiments. *Phys. Rev. Lett.* **96,** 108101.
Dudko, O. K., Mathe, J., Szabo, A., Meller, A., and Hummer, G. (2007). Extracting kinetics from single-molecule force spectroscopy: Nanopore unzipping of DNA hairpins. *Biophys. J.* **92,** 4188–4195.
Dudko, O. K., Hummer, G., and Szabo, A. (2008). Theory, analysis, and interpretation of single-molecule force spectroscopy experiments. *Proc. Natl. Acad. Sci. USA* **105,** 15755–15760.
Florin, E. L., Moy, V. T., and Gaub, H. E. (1994). Adhesion forces between individual ligand–receptor pairs. *Science* **264,** 415–417.
Fologea, D., Gershow, M., Ledden, B., McNabb, D. S., Golovchenko, J. A., and Li, J. L. (2005). Detecting single stranded DNA with a solid state nanopore. *Nano Lett.* **5,** 1905–1909.
Gautel, M., Oesterhelt, F., Fernandez, J. M., and Gaub, H. E. (1997). Reversible unfolding of individual titin immunoglobulin domains by AFM. *Science* **276,** 1109–1112.
Gershow, M., and Golovchenko, J. A. (2007). Recapturing and trapping single molecules with a solid-state nanopore. *Nat. Nanotechnol.* **2,** 775–779.
Greenleaf, W. J., Frieda, K. L., Foster, D., Woodside, M. T., and Block, S. M. (2008). Direct observation of hierarchical folding in single riboswitch aptamers. *Science* **319,** 630–633.
Heng, J. B., Ho, C., Kim, T., Timp, R., Aksimentiev, A., Grinkova, Y. V., Sligar, S., Schulten, K., and Timp, G. (2004). Sizing DNA using a nanometer-diameter pore. *Biophys. J.* **87,** 2905–2911.
Hornblower, B., Coombs, A., Whitaker, R. D., Kolomeisky, A., Picone, S. J., Meller, A., and Akeson, M. (2007). Single-molecule analysis of DNA–protein complexes using nanopores. *Nat. Methods* **4,** 315–317.
Jan Bonthuis, D., Zhang, J., Hornblower, B., Mathe, J., Shklovskii, B. I., and Meller, A. (2006). Self-energy-limited ion transport in subnanometer channels. *Phys. Rev. Lett.* **97,** 128104.
Kang, X. F., Cheley, S., Guan, X. Y., and Bayley, H. (2006). Stochastic detection of enantiomers. *J. Am. Chem. Soc.* **128,** 10684–10685.
Kasianowicz, J., Brandin, E., Branton, D., and Deamer, D. (1996). Characterization of individual polynucleotide molecules using a membrane channel. *Proc. Natl. Acad. Sci. USA* **93,** 13770–13773.
Kasianowicz, J. J., Kellermayer, M., and Deamer, D. W. (eds.) (2002). Structure and Dynamics of Confined Polymers, Springer, Dordrecht.
Kellermayer, M. S. Z., Smith, S. B., Granzier, H. L., and Bustamante, C. (1997). Folding–unfolding transitions in single titin molecules characterized with laser tweezers. *Science* **276,** 1112–1116.
Kim, M.-J., Wanunu, M., Bell, C. D., and Meller, A. (2006). Rapid fabrication of uniform size nanopores and nanopore arrays for parallel DNA analysis. *Adv. Mater.* **18,** 3149–3153.
Kramers, H. A. (1940). Brownian motion in a field of force and the diffusion model of chemical reactions. *Physica* **7,** 284–304.
Li, J., Stein, D., McMullan, C., Branton, D., Aziz, M. J., and Golovchenko, J. A. (2001). Ion-beam sculpting at nanometre length scales. *Nature* **412,** 166–169.
Liphardt, J., Onoa, B., Smith, S. B., Tinoco, I. J., and Bustamante, C. (2001). Reversible unfolding of single RNA molecules by mechanical force. *Science* **292,** 733–737.

Marszalek, P. E., Lu, H., Li, H., Carrion-Vazquez, M., Oberhauser, A. F., Schulten, K., and Fernandez, J. M. (1999). Mechanical unfolding intermediates in titin modules. *Nature* **402,** 100–103.

Mathé, J., Visram, H., Viasnoff, V., Rabin, Y., and Meller, A. (2004). Nanopore unzipping of individual DNA hairpin molecules. *Biophys. J.* **87,** 3205–3212.

Mathé, J., Arinstein, A., Rabin, Y., and Meller, A. (2006). Equilibrium and irreversible unzipping of DNA in a nanopore. *Europhys. Lett.* **73,** 128–134.

McNally, B., Wanunu, M., and Meller, A. (2008). Electro-mechanical unzipping of individual DNA molecules using synthetic sub-2 nm pores. *Nano Lett.* **8,** 3418–3422.

Meller, A. (2003). Dynamics of polynucleotide transport through nanometre-scale pores. *J. Phys.: Condens Matter* **15,** R581–R607.

Meller, A., Nivon, L., Brandin, E., Golovchenko, J., and Branton, D. (2000). Rapid nanopore discrimination between single polynucleotide molecules. *Proc. Natl. Acad. Sci. USA* **97,** 1079–1084.

Meller, A., Nivon, L., and Branton, D. (2001). Voltage-driven DNA translocations through a nanopore. *Phys. Rev. Lett.* **86,** 3435–3438.

Merkel, R., Nassoy, P., Leung, A., Ritchie, K., and Evans, E. (1999). Energy landscapes of receptor–ligand bonds explored with dynamic force spectroscopy. *Nature* **397,** 50–53.

Sauer-Budge, A. F., Nyamwanda, J. A., Lubensky, D. K., and Branton, D. (2003). Unzipping kinetics of double-stranded DNA in a nanopore. *Phys. Rev. Lett.* **90,** 238101.

Schlierf, M., and Rief, M. (2006). Single-molecule unfolding force distributions reveal a funnel-shaped energy landscape. *Biophys. J.* **90,** L33–L35.

Schlierf, M., Li, H. B., and Fernandez, J. M. (2004). The unfolding kinetics of ubiquitin captured with single-molecule force-clamp techniques. *Proc. Natl. Acad. Sci. USA* **101,** 7299–7304.

Smeets, R. M. M., Kowalczyk, S. W., Hall, A. R., Dekker, N. H., and Dekker, C. (2009). Translocation of RecA-coated double-stranded DNA through solid-state nanopores. *Nano Lett.* **9,** 3089–3095.

Song, L., Hobaugh, M. R., Shustak, C., Cheley, S., Bayley, H., and Gouax, J. E. (1996). Structure of staphylococcal α-hemolysin a heptameric transmembrane pore. *Science* **274,** 1859–1865.

Storm, A. J., Chen, J. H., Ling, X. S., Zandbergen, H. W., and Dekker, C. (2003). Fabrication of solid-state nanopores with single-nanometre precision. *Nat. Mater.* **2,** 537–540.

Storm, A. J., Chen, J. H., Zandbergen, H. W., and Dekker, C. (2005). Translocation of double-strand DNA through a silicon oxide nanopore. *Phys. Rev. E* **71,** 051903.

Wanunu, M., and Meller, A. (2008). Single-molecule analysis of nucleic acids and DNA–protein interactions using nanopores. *In* "Single-Molecule Techniques: A Laboratory Manual," (P. Selvin and T. J. Ha, eds.), pp. 395–420. Cold Spring Harbor Laboratory Press, Cold Spring Harbor, NY.

Wanunu, M., Morrison, W., Rabin, Y., Grosberg, A. Y., and Meller, A. (2010). Electrostatic Focusing of Unlabeled DNA into Nanoscale Pores using a Salt Gradient. *Nature Nanotech.* **5,** 160–165.

Wanunu, M., Sutin, J., McNally, B., Chow, A., and Meller, A. (2008). DNA translocation governed by interactions with solid state nanopores. *Biophys. J.* **95,** 4716–4725.

Wanunu, M., Sutin, J., and Meller, A. (2009). DNA profiling using solid-state nanopores: Detection of DNA-binding molecules. *Nano Lett.* **9,** 3498–3502.